Front. Environ. Sci. Eng. 2024, 18(1): 7
https://doi.org/10.1007/s11783-024-1767-8

RESEARCH ARTICLE

Direct generation of Zn metal using laser-induced ZnS to eradicate carbon emissions from electrolysis Zn production

Ying Chen[1,2], Ning Duan (✉)[1,2], Linhua Jiang (✉)[1,2], Fuyuan Xu[1,2], Guangbin Zhu[3], Yao Wang[1,2], Yong Liu[4], Wen Cheng[1,2], Yanli Xu[1,2]

1 State Key Laboratory of Pollution Control and Resources Reuse, College of Environmental Science and Engineering, Tongji University, Shanghai 200092, China
2 Shanghai Institute of Pollution Control and Ecological Security, Shanghai 200092, China
3 School of Environmental Science and Engineering, Tianjin University, Tianjin 300350, China
4 School of Materials Science and Engineering, Anhui University of Science & Technology, Huainan 232001, China

HIGHLIGHTS

- An optical metallurgy is proposed to directly generate Zn^0 from ZnS using laser.
- Zn^0 and S_8 can be detected on the surface of ZnS at a high laser fluence.
- The generation mechanism of Zn^0 and S_8 was explored.
- Providing a new way of producing high-purity metal without carbon emissions.
- A new method is proposed to promote the environmental goal of carbon neutrality.

GRAPHIC ABSTRACT

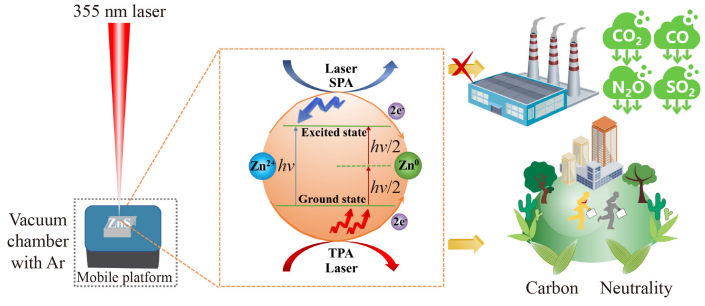

ABSTRACT

In response to the goal of net-zero emissions proposed by Intergovernmental Panel on Climate Change, Chinese government has pledged that carbon emissions will peak by 2030, and achieve carbon neutrality by 2060. However, the high carbon energy structure of traditional industries has aggravated environmental problems, such as greenhouse effect and air pollution. The goal of carbon neutrality will be difficult to achieve without the development of disruptive theories and technologies. The electrolytic zinc industry requires high-temperature roasting at ~1000 °C, generating large amounts of greenhouse gases and SO_2. High concentrations of sulfuric acid (200 g/L) are subsequently used for electrolysis, and each ton of zinc produced generates 50 kg of anode slime with lead content of up to 16%, as well as 0.35 m^3 of wastewater containing zinc and lead. To solve these problems, an optical metallurgy method is proposed in this study. The proposed method uses laser-induced photoreduction to decompose ZnS and reduce metal ions to metal. Results indicate that Zn^0 and S_8 can be detected on the surface of ZnS at a specific wavelength and laser fluence. The generation mechanism of Zn^0 is such that laser induces an electronic transition that breaks ionic bond in ZnS, resulting in its decomposition and photoreduction to Zn^0 under an inert argon gas atmosphere. This method does not reduce other metals in the mineral since it does not use high-temperature roasting, providing a new way of producing high-purity metal without greenhouse gas emissions and heavy metal pollution caused by traditional zinc electrolysis.

ARTICLE INFO

Article history:
Received 6 March 2023
Revised 5 July 2023
Accepted 11 July 2023
Available online 17 August 2023

Keywords:
Laser metallurgy
ZnS
Photochemical reduction
Zinc

✉ Corresponding authors
E-mails: ningduan@tongji.edu.cn (N. Duan);
jianglinhua@tongji.edu.cn (L. Jiang)

Special Issue—Visions

1 Introduction

China is the world's largest emitter of CO_2, accounting for a third of global carbon emissions (Yang et al., 2022).

In response to the goal of net-zero emissions proposed by the Intergovernmental Panel on Climate Change, the Chinese government formally proposed at the 75th session of the UN general assembly the goal of "striving to peak CO_2 emissions before 2030 and reaching carbon neutrality before 2060" (Zhang et al., 2022a). However, the non-ferrous metallurgical industry is crucial to economic development in China, and requires large amounts of energy that produce large quantities of carbon emissions. According to the China Non-ferrous Metals Industry Association, carbon dioxide emissions from the non-ferrous industry will reach 660 million tons in 2020, accounting for 4.7% of China's total emissions with a peak expected to reach 750 million tons. Heavy metal wastewater emissions from this industry are the highest among all industries in China. Due to the large amount of greenhouse gases emitted during production, traditional industries will not be able to achieve their strategic goal of carbon neutrality and solve the pollution problem at the source without the development of disruptive theories and technologies.

Zinc is one of the most popular and versatile metals, with a wide range of applications in construction, shipping, food, electronics, biological engineering, pharmaceuticals, and cosmetics, among other industries. Production processes for over 85% of zinc include roasting and electrolytic zinc. The roasting process requires high temperatures of ~1000 °C, which consumes huge amounts of fossil fuel energy and releases large amounts of carbon dioxide. In 2020, the process of producing one ton of zinc in China's zinc metallurgy industry produced carbon dioxide emissions of 5.19 t, which is equivalent to 1.9 t of standard coal consumption. The zinc industry, with a total carbon dioxide emission of 33 million tons, is a major driver of greenhouse gas emissions. For instance, the amount of global warming potential caused by global zinc production was 0.04 Gt carbon dioxide (CO_2) in 2008, incurring a huge environmental burden (Qi et.al, 2017). It is estimated that the electrolytic zinc industry in China produces ~6,000,000 t of solid waste each year, which is classified as hazardous waste due to its high heavy metal content. Each ton of zinc produced generates 50 kg of anode slime with up to 16% lead content, a ton of acid leach residue, and 0.35 m^3 of high zinc and high lead wastewater, the high toxicity of which causes environmental pollution and significant health risks (Luo et.al, 2019).

To solve the above problems in electrolytic zinc production, researchers have developed various technologies with considerable success. Ale Ebrahim and Jamshidi (2004) combined metallurgical units with petrochemical units, which use the reaction of zinc oxide with methane to simultaneously produce metallic zinc and synthesis gas; synthesis gas can be used to make petrochemical products, thereby eliminating the greenhouse gas emissions from a conventional zinc production plant. Griessacher et al. (2012) utilized charcoal as an alternative reducing agent to achieve an almost complete reduction of zinc oxide and zinc volatilization when reduced with charcoal, which offers a higher reducing capacity and reduced greenhouse gas emissions when compared to fossil coals and coke. Omran et al. (2018) reduced zinc oxide to pure zinc using microwave-based heating technology, which has a high heating rate and short heating time, reducing energy consumption and carbon emissions compared to traditional zinc metallurgy methods. Chuayboon and Abanades (2023) converted sunlight into an energy-intensive chemical fuel, which uses solar energy to drive the carbon-thermal reduction of zinc oxide for high-purity zinc production using bio-sourced reducers as carbon sources in the process, reducing the dependence on fossil fuels and decreasing greenhouse emissions. However, these technologies are improvements to existing processes whose reductions in carbon emissions from the electrolytic zinc industry are far from sufficient to achieve carbon neutrality.

In this study, we propose a new optical metallurgy method, which uses laser-induced photoreduction to decompose ZnS and reduce metal ions to metal. Du and Ren (1995) studied the interaction between the laser source and tin concentrate. In their study, tin metal was directly detected by uniformly scanning the entire tin concentrate powder with a laser. Recently, Jiang et al. (2019) explored nanoscale laser metallurgy. They showed that a laser accurately delivered patches of highly concentrated energy to the metal ions in the crystals of metal-organic frameworks (MOF), which were transformed into carbonaceous organic linkers, resulting in the formation of reductive species, which in turn reduced the metal ions into atoms. The results of our study indicate that Zn^0 and S_8 can be detected on the surface of ZnS at a specific wavelength and laser fluence. The generation mechanism of Zn^0 is such that the laser induces an electronic transition that breaks the ionic bond in ZnS, resulting in its decomposition and photoreduction to Zn^0 under an inert argon gas atmosphere. This method does not reduce other metals in the mineral since it does not use high-temperature roasting, providing a new way of producing high-purity metal without greenhouse gas emissions and heavy metal pollution caused by traditional zinc electrolysis.

2 Materials and methods

2.1 Materials

Sphalerite (ZnS) is the primary source used in the electrolytic zinc industry. It is difficult to observe the changes in the surface morphology when ZnS powder was directly used for characterization. Therefore, the sample used for our experiments was ZnS wafer purcha-

sed from Guangzhou Hengyang Electronic Technology Co. Ltd. (Guangdong, China). The ZnS wafer was round, 12.7 mm in diameter, and 2 mm thick (Fig. S1).

2.2 Characterization and identification

2.2.1 Characterizations

Atomic force microscopy (AFM) was conducted using a Bruker Dimension Icon instrument equipped with a Nanoscope V controller, and was used to measure the roughness of ZnS powder and ZnS wafer to determine the materials required for our experiments. Scanning electron microscopy (SEM) images were recorded on a Germany ZEISS Gemini SEM 300 instrument, which were used to observe the changes in the surface morphology of ZnS after laser irradiation and explain the generation mechanism of the obtained products.

2.2.2 Identification of the products

The Raman spectra were obtained on a Renishaw in Via laser Raman spectrometer equipped with a 100× magnification objective and excited using a solid-state laser source operated at an excitement wavelength of 515 nm to determine the types of products formed during the laser irradiation of ZnS. The chemical states of the ZnS samples obtained after laser irradiation were characterized on a Thermo Scientific K-Alpha X-ray photoelectron spectrometer using a monochromatic Al-Kα X-ray radiation source at an energy resolution of 0.1 eV, background pressure of 3×10^{-8} Pa, and background subtraction of smart. The Zn species in the solid phase were quantified by linear combination fitting (LCF) analysis of the Zn k^3-weighted extended X-ray absorption fine structure (EXAFS, SSRF) spectra. It was performed with Si(111) crystal monochromators at the BL14w and BL11b beamlines at the SSRF, Shanghai, China.

2.3 Laser-induced decomposition experiment

2.3.1 Construction of the experimental apparatus

The experimental platform used for the laser-induced decomposition of ZnS is mainly composed of an optical system, mechanical system, and control system, as shown in Fig. 1. The specific experimental instrument mainly includes a laser, lens, three-axis motorized stage, vacuum chamber, charge-coupled device (CCD) camera, and so on. The samples were placed process face up on a three-axis motorized stage with a 0.1 mm positional resolution capability in the horizontal plane direction. External computerized stage control allows for programming the total irradiation area, design of the path configuration to be irradiated, and the exposure time on each point along the path. A computer-controlled XY-stage (for sample) and Z-stage (for the lens) allowed for the precise

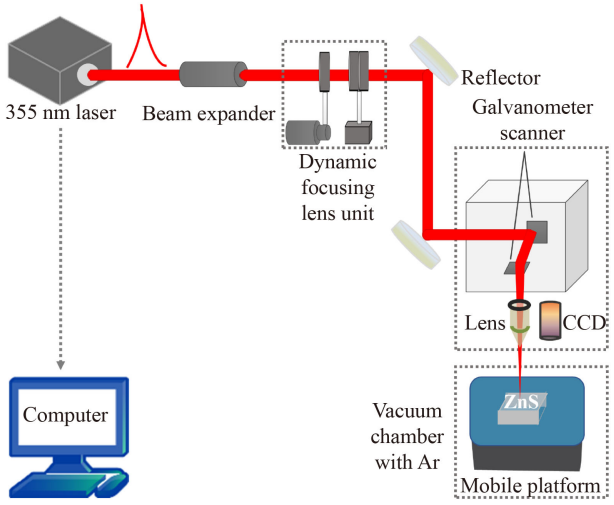

Fig. 1 Schematic diagram of the experimental apparatus used for the laser-induced decomposition of ZnS.

positioning of the spot on the sample surface and enabled us to scan the surface at 300 mm/s. The laser parameters were utilized to adjust the irradiation fluence and position of the laser spot on the ZnS sample, which was monitored *in situ* using a CCD camera. The images of each laser spot were collected by the CCD camera, especially the images of the transient state changes observed during the laser-induced decomposition of ZnS. At the same time, it was convenient to test the laser damage threshold for ZnS wafer.

To avoid the interference of oxygen, an inert argon gas protection device was set up for the laser-induced decomposition of ZnS. In this experiment, ZnS wafer was placed directly into a quartz sheet with a groove (purchased from Yixing Purshee Experiment Co. Ltd., Jiangsu, China), which was compacted with another quartz sheet of the same size and sealed with tape to isolate air as far as possible. Consequently, it was placed in a vacuum chamber and fixed to a quartz window with double-sided adhesive tape. After the samples were placed in the vacuum chamber, the vacuum was pumped and then filled with argon gas (purchased from Wuhan Xiangyun Industry and Trade Co. Ltd., Hubei, China). The vacuum was pumped and filled with argon gas for > 8 times to ensure that there was no oxygen in the vacuum chamber. The vacuum chamber was placed on a three-axis motorized stage with its surface perpendicular to the propagation direction of the laser beam, and a line scan was used for the laser-induced decomposition of ZnS. After the test, the samples were placed in the vacuum chamber for cooling. After the temperature of the samples gradually returned to room temperature, they were taken out and used to characterize the obtained products.

ZnS has attracted considerable research interest due to its high response to light. In particular, pure ZnS can only absorb ultraviolet light with a wavelength of < 380 nm (Feng et al., 2022). ZnS can be excited and produce

photogenerated electron–hole pairs under irradiation with light. Therefore, a nanosecond-pulsed ultraviolet laser (OPTOWAVE Co. Ltd., USA) with a wavelength of 355 nm was utilized to explore the types of product obtained during the laser-induced decomposition of ZnS under an inert argon gas atmosphere. For a pulsed laser, its parameters mainly include the laser fluence, laser power, scanning speed, scanning interval, pulse repetition frequency, light spot diameter, and so on. The spot diameter of the laser beam was ~40 um. The laser parameters were generally set according to the laser fluence, while the laser fluence is related to the laser power, pulse repetition frequency, and light spot area (Xiang et al., 2022).

$$F = \frac{P}{f \cdot S} = \frac{P}{f \cdot \pi \cdot \left(\frac{D}{2}\right)^2} = \frac{4P}{f \cdot \pi \cdot D^2}, \quad (1)$$

where F, P, f, S, D, and π are the laser fluence (J/cm^2), laser power (W), pulse repetition frequency (kHz), light spot area (cm^2), and light spot diameter (cm), and circumference ratio, respectively.

2.3.2 Laser-induced damage threshold experiment

In this paper, the laser-induced damage threshold of ZnS should be determined because only ZnS was damaged and ablated, and the mechanism of this ablation is thought to be photon absorption-induced. Therefore, during the laser-induced damage threshold experiment, a scanning speed of 300 mm/s, scanning interval of 0.01 mm, and light spot diameter of 40 μm were kept constant and the effect of the laser fluence explored in detail to determine the surface morphology damage threshold of ZnS.

The morphology of the laser-induced damage of ZnS was confirmed by the occurrence of the surface damaged sites observed using an online microscopic detection set-up consisting of a CCD camera and electron microscopy. Each site was irradiated with increasing laser fluence and could be defined as either damaged or undamaged using microscopy. The specific laser parameters used in our experiment are shown in Table S1.

2.3.3 Laser-induced decomposition of ZnS

Based on a preliminary single factor experiment, it was found that the laser fluence has the most significant effect on the surface micromorphology. Therefore, in the laser-induced damage threshold experiment, a scanning speed of 300 mm/s, scanning interval of 0.01 mm, and light spot diameter of 40 μm were used, and the effect of the laser fluence was explored in detail to determine the types of products formed via the laser-induced decomposition of ZnS.

According to the laser damage threshold of ZnS, the thermal effect generated by ZnS under different laser fluence, and the energy loss when the laser passed through the quartz window of the vacuum chamber and quartz sheet outside of the ZnS groove, the laser parameters used in the laser-induced decomposition of ZnS experiment were designed, as shown in Table S2.

Table S2 shows the surface damage and ablation of ZnS observed under the different laser parameters studied, and the products were identified to determine whether Zn^0 was generated in the process. In addition, the generation mechanisms of the different products were clarified based on the changes observed in the surface morphology of ZnS.

3 Results and discussion

3.1 The optimal absorption wavelength of ZnS

The energy-band structures of ZnS were elucidated using density functional theory (DFT) calculations to better explain the electron transition mechanism of ZnS and determine the maximum absorption wavelength. Our calculations were carried out using the CASTEP software package (Zhang et al., 2022b). In our calculations, the exchange correlation function used the mixed correction function of HSE06 of Heyd under Hybrid, which involves mixing of the Hartree–Fock non-local exchange and generalized gradient approximation (GGA) exchange to compensate for the underestimation of the band gap of DFT. Norm-conserving was used to describe the interaction between the solid ions and valence electrons. After the convergence test of the cut-off energy, all calculations were carried out in the reciprocal space.

Figure 2 shows the energy band structures of ZnS obtained using DFT calculations. The energy band of ZnS was divided into upper and lower parts with the Fermi level (E_F = 0) as the boundary. The upper part was divided into the conduction band, which is not occupied by valence electrons, and the lower part was divided into the valence band, which is occupied by valence electrons. The band gap was between the conduction and valence bands, and its value was 2.978 eV, which is less than the experimental value of 3.6 eV (Kumar and Rao, 2022). Scissors was used to correct the band gap and set as 0.7 eV. The final simulation result was 3.678 eV, which is similar to the experimental value (3.6 eV).

Figure 2 shows the x-coordinate represents the high symmetry point in the Brillouin region, the y-coordinate represents the energy value, and each line in the diagram corresponds to a track. The energy band of ZnS was divided into two parts with the Fermi-level as the boundary; the CBM represents the minimum conduction band, VBM represents the maximum valence band, and its band gap was 3.678 eV. Figure 2 shows both the top of the valence band and the bottom of the conduction band of ZnS were at high symmetry point G, indicating that ZnS was a direct band gap semiconductor, which is more

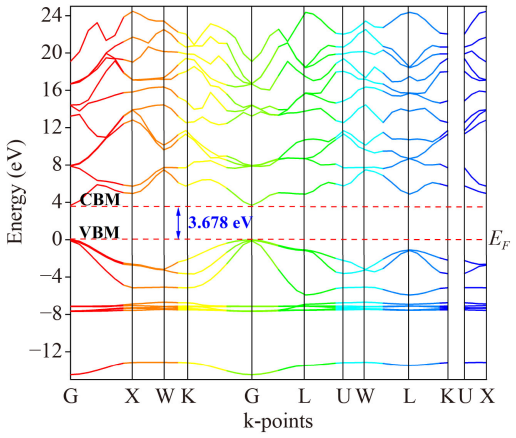

Fig. 2 Diagram of the band structure of cubic ZnS.

prone to electronic transition (Jiang et al., 2023). As there is only an energy change before and after the electronic transition in a direct band gap semiconductor and no change in its position, there is a greater chance that energy will be released in the form of photons.

The band gap of ZnS was 3.678 eV according to the photoenergy shown in Eq. (2).

$$E = h\nu = \frac{hc}{\lambda}, \tag{2}$$

where E is the energy (J), $h\nu$ is Planck's constant (6.63×10^{-34} J·s), c is the speed of light (3×10^{17} nm/s), and λ is the laser wavelength (nm).

According to Eq. (2), the maximum absorption wavelength of ZnS was obtained as 337 nm. ZnS is a direct band gap semiconductor, which is easy to transfer from its highest occupied state to the lowest vacant orbital, so it is easily detected using instruments. For example, the ability of ZnS to absorb light at different excitation wavelengths can be obtained using UV-visible-NIR diffuse reflectance spectroscopy. That is, the optimal absorption wavelength range where ZnS was most prone to electronic transition can be determined.

Figure S2 shows that ZnS has a relatively low absorption intensity in the visible light region and relatively high light response in the UV region, especially in the wavelength range of 290–360 nm with a strong light absorption intensity (⩾ 66.9%). Due to 337 nm UV lasers being rarely used in the market, a UV nanosecond laser with a wavelength of 355 nm was selected in this paper to study the laser-induced decomposition of ZnS. The single-photon energy of the laser was ~3.5 eV, which is similar to the band gap of ZnS. Therefore, ZnS was able to absorb the photon energy of this laser via a single or two-photon pathway.

3.2 The laser-induced damage of ZnS

The micromorphology of the laser-induced damage of ZnS was characterized using a CCD camera and electron microscopy, as shown in Fig. S3. When the laser fluence was ⩽ 0.33 J/cm^2, the morphology of ZnS did not change significantly. However, when the laser fluence was 0.37 J/cm^2, laser damage occurred on the ZnS surface. When the laser fluence reached 0.43 J/cm^2, the overall surface morphology of ZnS was damaged, and with an increase in the laser fluence, this damage gradually increased and became laser ablation. Therefore, the maximum damage threshold for ZnS wafer was 0.33 J/cm^2. It can be seen from the above studies that the design of the laser parameters used for the laser-induced decomposition of ZnS should be based on the laser damage threshold and the laser fluence should be gradually increased to ensure that ZnS can absorb the photon energy. Thus, the surface morphology and chemical composition of ZnS were changed and the decomposition of Zn^{2+} into Zn^0 was achieved via a photoreduction process.

3.3 Identification and mechanistic analysis of the products

3.3.1 Results analysis of Raman spectroscopy

The Raman spectra of the laser treated ZnS surface were acquired and compared to the Raman signals observed for the native material to determine whether the new products were generated.

Figure 3(a) shows the Raman spectrum obtained for the original ZnS wafer exhibits vibrational modes at 216, 271, 346, 416, and 667 cm^{-1}. The broad intense peak at 346 cm^{-1}, which is the characteristic Raman scattering peak of ZnS, can be indexed to the longitudinal optical (LO) polar phonon mode of vibration (Naik et al., 2021). Low intensity peaks were also observed at 216 and 271 cm^{-1} corresponding to the transverse optical (TO) phonon and longitudinal acoustic (LA) phonon modes, respectively (Roychowdhury et al., 2014). Another small peak observed at 416 cm^{-1} was attributed to the first order and second zone-boundary phonons. In addition, a small peak observed at 667 cm^{-1} in the inset of Fig. 3(a) was attributed to the second order optical phonon (2LO) (Scocioreanu et al., 2012).

When compared with the original ZnS sample, new Raman peaks appear in the Raman spectrum obtained for ZnS after the laser-induced decomposition process. In Fig. 3(b), a new moderately intense peak appeared at 466 cm^{-1} when the laser fluence was 4.11 J/cm^2 at a pulse repetition frequency of 60 kHz, which was attributed to S_8, indicating that a new substance was generated during the interaction between ZnS and the laser (Shee et al., 2015). The mechanism for the generation of S_8 was as follows. Because the relative atomic mass of the S is less than Zn, it will be ejected after the absorption of the incident laser energy. The ionic bonds between the constituent atoms have some propensity to break, followed by the Zn atom that makes

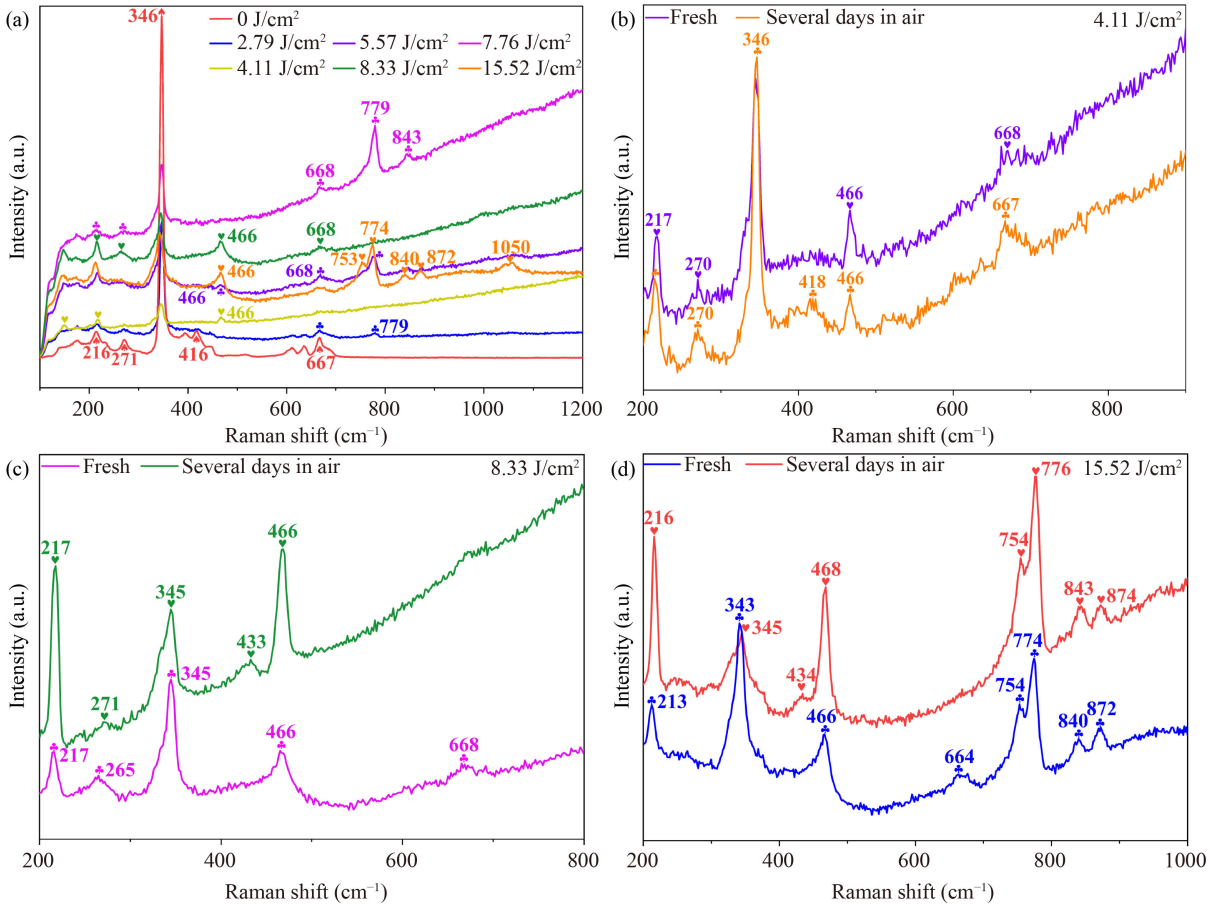

Fig. 3 The Raman spectra obtained for (a) the products formed using different pulse repetition frequency and laser fluence, (b–d) the fresh samples and samples exposed to air for several days under different laser fluence with a pulse repetition frequency of 60 kHz.

up the surface layer, and thus has dangling bonds (Major et al., 2014). Under the inert argon atmosphere, the S atoms are increasingly ejected after the absorption of the incident laser energy. Multiple S atoms collide with each other and bond with each other to form S_8. The sample was exposed to air for several days and then re-tested, and no new Raman peaks are observed, as shown in Fig. 3(b).

Figure 3(c) shows when the laser fluence was 8.33 J/cm^2, the Raman spectrum of ZnS exhibits a new peak at 466 cm^{-1}, which corresponds to the S-S stretching vibrations of S_8 (Shee et al., 2015). After exposing the sample to air for several days, it was found that a new small peak appeared at 433 cm^{-1}, which was attributed to ZnO (Achehboune et al., 2022). ZnS will not be oxidized to ZnO under an air environment at normal temperature and pressure, but Zn^0 will be slowly oxidized to ZnO in the air, making it impossible to exist in air for a long period of time. Therefore, it can be seen that a certain quantity of Zn^0 (metal has no Raman spectrum) was generated during the laser-induced decomposition of ZnS under an inert argon gas atmosphere, which will be slowly oxidized to ZnO after being exposed to air.

Figure 3(d) shows when the laser fluence was 15.52 J/cm^2, the Raman spectrum of ZnS has obvious new peaks at 466, 754, 774, 840, and 872 cm^{-1}. A strong Raman peak appeared at 466 cm^{-1}, which was attributed to S_8 (Shee et al., 2015). The other new peaks at 754, 774, 840, and 872 cm^{-1} were assigned to the recombination of ZnS (Keshav and Mg, 2018). This result suggests that under a high laser fluence, a large amount of ZnS was decomposed by the laser irradiation, and subsequent redeposition on the surface by annealing, resulting in more new Raman peaks. After exposing the sample to air for several days, it was found that there was a new small peak at 433 cm^{-1} corresponding to ZnO. This demonstrated that a certain quantity of Zn^0 was generated during the laser decomposition of ZnS under an inert argon atmosphere, which was oxidized to ZnO after being exposed to air (Achehboune et al., 2022).

When the pulse repetition frequency was 20 kHz, the Raman spectrum of ZnS exhibits an obvious new peak near 774 cm^{-1} at a laser fluence of 2.79, 5.57, and 7.76 J/cm^2, which was attributed to ZnS (Keshav and Mg, 2018). This was attributed to most of the decomposed ZnS being recombined to generate ZnS under irradiation with this set of parameters. At a laser fluence of

7.76 J/cm^2, ZnS exhibits new Raman peaks at 774, 779, and 843 cm^{-1}, all of which were assigned to recombine ZnS after laser decomposition. Moreover, the intensity of the Raman peak was significantly higher than the peak value observed at a laser fluence of 2.79 and 5.57 J/cm^2, proving that more and more ZnS was decomposed by the laser as the laser fluence increases (Keshav and Mg, 2018). Due to the laser fluence at a pulse repetition frequency of 20 kHz being less than that at a pulse repetition frequency of 60 kHz, the amount of S_8 generated during the laser-induced decomposition of ZnS was less, resulting in no significant new peaks.

In conclusion, the Raman peak of S_8 appears at different laser fluence for the products not exposed to air at a pulse repetition frequency of 60 kHz, while no other new substances appear. When the laser fluence was 8.33 and 15.52 J/cm^2, the Raman peak of ZnO appear after the sample was exposed to air for several days, indicating that a certain quantity of Zn^0 was generated during the laser-induced decomposition of ZnS under an inert argon gas atmosphere, which will be oxidized to ZnO after being exposed to air. No new substances were generated due to the relatively small laser fluence at a pulse repetition frequency of 20 kHz, indicating that the laser-induced photoreduction of ZnS can only occur under the irradiation at a high laser fluence.

3.3.2 XPS analysis and generation mechanism for the products

XPS analysis of the products was carried out in order to further investigate the surface composition and chemical state of ZnS. All of the binding energies of all elements were calibrated using the C 1s peak observed at 284.8 eV. The difference of ~23 eV between two core level components of $Zn_{2p3/2}$ and $Zn_{2p1/2}$ and 1.2 eV of $S_{2p3/2}$ and $S_{2p1/2}$. The deconvolution of the spectra was made using mixed Gaussian–Lorentzian functions with an iterative least-squares computer program. The values of full width at half maximum (FWHM) were kept equal between 1.2 and 2.0 eV, and the Gaussian–Lorentzian ratio was 30%. To provide chemical environmental information, a narrow scan was performed for certain elemental core levels with a pass energy of 50 eV to obtain the high-resolution spectra.

Figure S4 shows XPS survey spectra of the original sample and those after the laser irradiation of ZnS at different pulse repetition frequencies and laser fluence. According to Figs. S4(a) and S4(b), the XPS spectra consist of the peaks corresponding to Zn 2p, S 2p, O 2p, and C 1s, indicating that no other impurities were doped in the samples. Therefore, Zn and S were analyzed and the chemical states and surface composition investigated. The purpose of this paper was to determine whether Zn^0 exists in the products obtained during the laser-induced decomposition of ZnS; Zn element should be analyzed to determine its chemical state and composition.

Two peaks corresponding to the Zn 2p XPS spectrum of the original ZnS sample (Fig. 4(a)) were observed at binding energies of 1022.1 and 1022.8 eV. The peak at 1022.1 eV originates from the Zn-S bond (Zhou et al., 2022). The binding energy value observed for Zn 2p (1022.8 eV) was similar to the value reported in the NIST XPS database and was attributed to $ZnSO_4$, indicating that a certain quantity of ZnS was converted into $ZnSO_4$ after long-term exposure to an air environment (Wagner et al., 2012).

Figures 4(b) and 4(c) show the binding energies observed for Zn 2p were 1022.1 and 1022.2 eV, which correspond to Zn-S, yet no Zn^0 was produced when the pulse repetition frequency was 20 kHz and the laser fluence was 2.79 and 5.57 J/cm^2. The presence of two chemical environments including Zn-S and Zn^0 was evidenced by the peaks observed for Zn 2p at 1022.2 and 1021.9 eV, as shown in Fig. 4(d) (Young Maeng et al., 2023). These results prove that a certain quantity of ZnS will be photoreduced to Zn^0 upon laser decomposition at a high laser fluence with a Zn^{2+}:Zn^0 atomic ratio of 94.06:5.94.

Figure 5(b) shows the binding energy at 1022.1 eV was attributed to the Zn-S bond, showing that Zn^0 was not generated at a laser fluence of 4.11 J/cm^2 and a pulse repetition frequency of 60 kHz. From the Zn 2p spectrum (Fig. 5 (c)), the corresponding two peaks observed at 1022.2 and 1021.9 eV were assigned to Zn-S and Zn^0, respectively when the laser fluence was 8.33 J/cm^2 (Young Maeng et al., 2023). The results show that a certain amount of ZnS will undergo laser-induced decomposition, resulting in the photoreduction of Zn^{2+} to Zn^0 with a Zn^{2+}:Zn^0 atomic ratio of 91.86:8.14. In Fig. 5(d), the signals corresponding to Zn 2p were probed in the XPS spectra at 1022.2 eV and 1021.9 eV, which are assigned to Zn-S and Zn^0, indicating that a certain quantity of ZnS was photoreduced to Zn^0 upon laser decomposition at a laser fluence of 15.52 J/cm^2 (Young Maeng et al., 2023). The quantification of these peaks reveals that the atomic ratio of Zn^{2+} to Zn^0 was 91.6:8.4.

The atomic ratios of Zn^{2+} and Zn^0 for laser-induced decomposition of ZnS at different laser fluence are shown in Fig. 6.

Figure 6 shows it is difficult for the laser to induce the decomposition of ZnS to generate Zn^0 at a low laser fluence, regardless if the pulse repetition frequency was 20 or 60 kHz, while Zn^0 is gradually generated in the products of laser-induced decomposition of ZnS upon increasing the laser fluence. Meanwhile, the amount of Zn^0 generated via the laser-induced decomposition of ZnS gradually increases upon increasing the laser fluence at a pulse repetition frequency of 60 kHz, while the amount of Zn^0 does not change significantly as the laser fluence reaches a certain level.

During the interaction of the laser with a semiconduc-

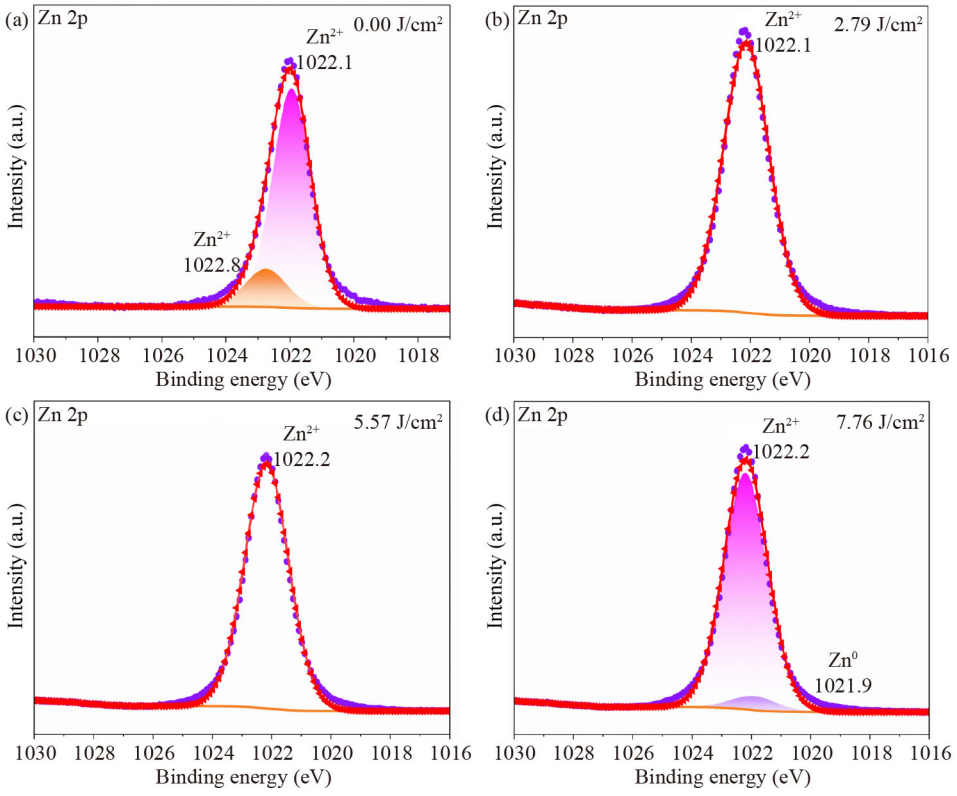

Fig. 4 XPS spectra obtained for Zn at a pulse repetition frequency of 20 kHz with different laser fluence: (a) Zn 2p, 0.00 J/cm^2; (b) Zn 2p, 2.79 J/cm^2; (c) Zn 2p, 5.57 J/cm^2; (d) Zn 2p, 7.76 J/cm^2.

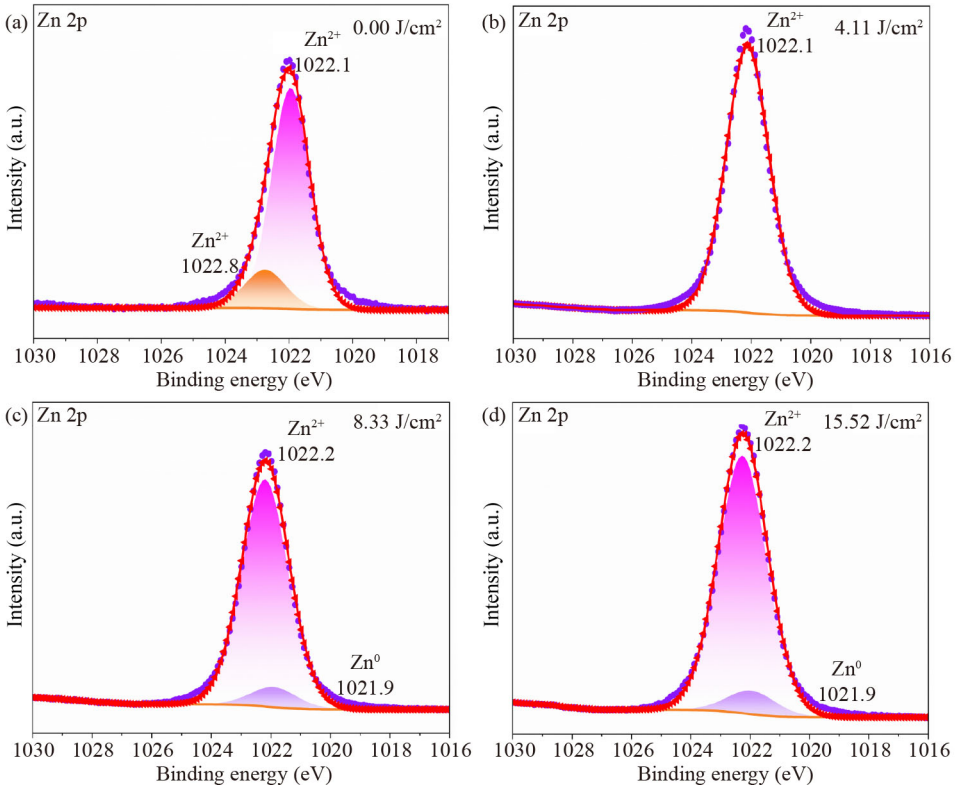

Fig. 5 XPS spectra obtained for Zn at a pulse repetition frequency of 60 kHz with different laser fluence: (a) Zn 2p, 0.00 J/cm^2; (b) Zn 2p, 4.11 J/cm^2; (c) Zn 2p, 8.33 J/cm^2; (d) Zn 2p, 15.52 J/cm^2.

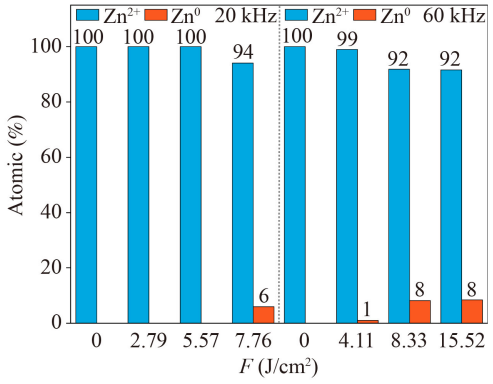

Fig. 6 Atomic ratio of Zn^{2+} and Zn^0 at different laser fluence

tor, the bound electrons in the valence band absorb photon energy via electron-beam heating and electron excitation, which can excite and induce an electron transition. This electron transition ionizes some of the bound electrons in the valence band. This causes them to be excited to the conduction band, increasing the carrier density on the semiconductor surface. The carriers absorb the energy of the incident laser photons and diffuse into the material, which improves the temperature of the semiconductor lattice and enables the transfer of photon energy to the semiconductor lattice system. The metal ions are reduced to metal upon absorbing enough photon energy via single or multiple photons. The laser reduction reaction is divided into photochemical reduction and photothermal reduction with the advantages of safety, stability, and easy regulation. As the laser is irradiated on the sample, if the photon energy is greater than the band gap ($hv > Eg$), it will excite an electron to transfer from the valence band to conduction band, and an electron-hole pair generated via photon-excitation (Zhang et al., 2020). The free electrons interact with the oxygen-containing functional groups or other substances to undergo a photochemical reaction, whereby the photon energy breaks the ionic bonds prior to heat transfer. When the photon energy is less than the band gap ($hv < Eg$), the electron will not transfer, but with an increase in the laser fluence, the absorption of photons will increase, which will enhance the molecular and lattice vibrations. The irradiated area is instantaneously heated to high temperatures, breaking the chemical bond, followed by the photothermal reduction reaction (Okano et al., 2016). The single-photon energy of the laser used in this experiment was ~3.5 eV, which is similar to the band gap of ZnS (3.678 eV), while ZnS is a semiconductor that can theoretically absorb the photon energy of the laser via single or two-photon pathways (Fig. 7) (Kumar et al., 2023). The reason for the generation of Zn^0 was that photons play the role of energy carriers and transfer energy to the surface of ZnS, followed by the free electrons on the surface absorbing the photon energy and undergo transition. Subsequently, the ionic bonds in ZnS are broken along with the Zn atoms being ejected and bonding with each other to form Zn^0 under the inert argon gas atmosphere. During the photoreduction process of the laser-induced decomposition of ZnS to Zn^0, the photochemical effect was dominant (Ye et al., 2021). At a high laser fluence of 15.52 J/cm^2, the surface micromorphology of ZnS after laser irradiation shows that there was no burrs or deformation around the ablated region, as shown in Fig. S5, indicating that there was no obvious photothermal phenomenon, which corresponds to the photochemical mechanism of the interaction between the laser and substance. This is because the ionic bonds in ZnS were broken during the photochemical reaction, as was described earlier.

Since the laser used in this experiment was a nanosecond ultraviolet laser with a relatively large pulse width, thermal evaporation occurs when irradiating the solid substance, which can produce a strong photothermal effect. The photon energy will be transferred and accumulated in the materials matrix, followed by the rate of conversion of photon energy into heat being faster than the rate of the chemical reaction, resulting in the absorbed

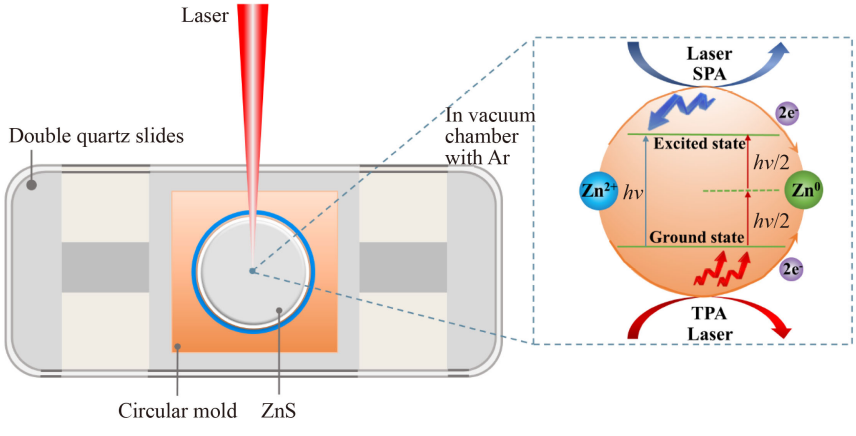

Fig. 7 Schematic representation of single-photon and two-photon absorption during the laser-induced decomposition of ZnS.

photon energy being converted into molecular vibration energy. The vibration energy turns into heat energy, which makes the surface temperature of substance increase. When temperature rises to a certain extent, it will also cause thermal cracking of the ionic bonds, melting, and even vaporization of the materials surface, causing changes in the chemical composition on the surface. The nanosecond laser may produce part of the photothermal effect leading to the generation of Zn^0 during the laser-induced decomposition of ZnS. Therefore, the generation mechanism of Zn^0 is a synergistic photochemical and photothermal mechanism, while the photochemical effect is more intense (Feng et al., 2000).

To further determine the types of product, the surface composition and chemical state of S was analyzed in this study.

Figs. S6(a) and 8(a) show that the S 2p spectrum of the original ZnS. The binding energy peaks observed at 161.6 and 162.9 eV can be attributed to the S-Zn bonds (Yang et al., 2023). The binding energy values observed for S 2p at 168.6 and 169.8 eV were similar to the values reported in the NIST XPS database and were attributed to $ZnSO_4$, revealing that a certain quantity of ZnS was converted into $ZnSO_4$ after long-term expose to an air environment (Wagner et al., 2012).

However, when ZnS was irradiated with different laser fluence, four peaks corresponding to S 2p (Figs. 8 and S6) were observed at 161.6, 162.1, 162.9, and 163.3 eV. The typical doublet of $S_{2p3/2}$ and $S_{2p1/2}$ (161.6 and 162.9 eV) was ascribed to S-Zn (Yang et al., 2023). In addition, the other peaks of $S_{2p3/2}$ and $S_{2p1/2}$ at 162.1 and 163.3 eV were observed, indicating the production of S-Zn (Waltrovitz et al., 2022).

The atomic ratios of the spin-orbital of S 2p were analyzed at different laser energy densities, and the results were as follows. As can be seen from Fig. S7, with an increase in the laser fluence at the same pulse repetition frequency, all of the binding energies of S 2p (161.6 eV) gradually shift to relatively higher binding energies (163.3 eV) when compared with pure ZnS, demonstrating that more and more S atoms were ejected, resulting in the incorporation of more sulfur vacancies into the products (Meng et al., 2021). The laser irradiation can accelerate the transfer of electrons from the ZnS to sulfur vacancies and thus reduce the equilibrium electron cloud density, endowing the enhancement in the binding energies (Low et al., 2019). When combined with Fig. 6, the amount of Zn^0 increases with an increase of sulfur vacancies. The results prove that the S atoms will be ejected before Zn during the laser-induced decomposition of ZnS. When many S atoms are ejected, a certain

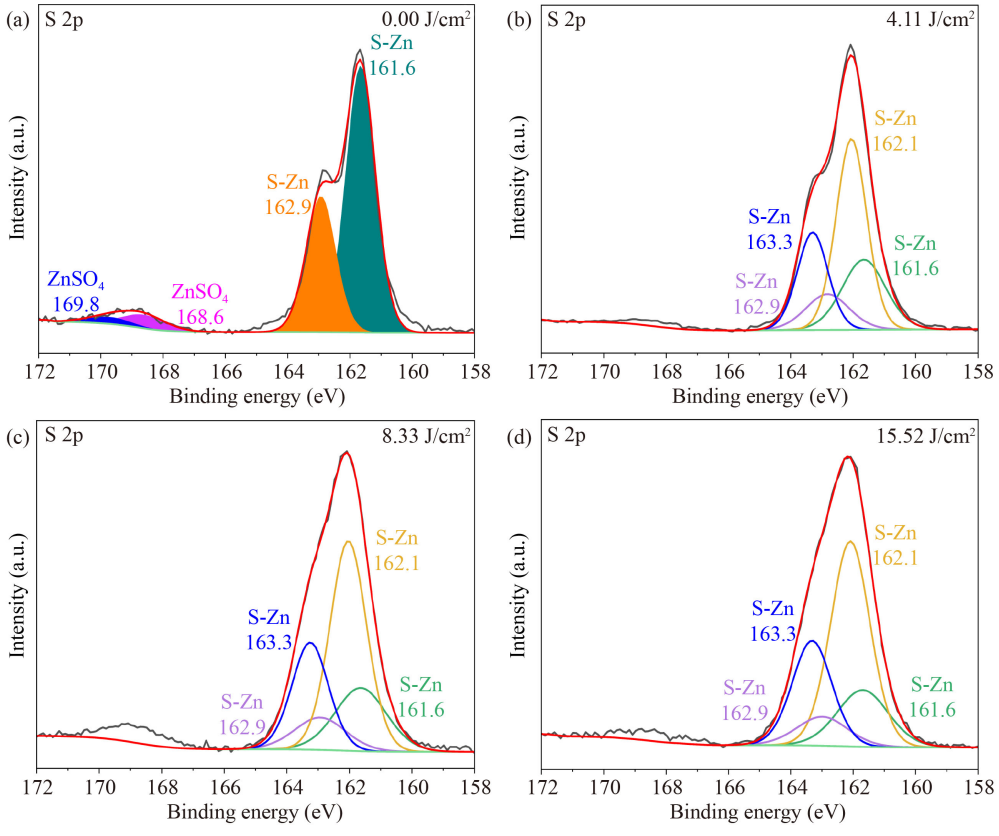

Fig. 8 XPS spectra obtained for S at a pulse repetition frequency of 60 kHz with different laser fluence: (a) S 2p, 0.00 J/cm^2; (b) S 2p, 4.11 J/cm^2; (c) S 2p, 8.33 J/cm^2; (d) S 2p, 15.52 J/cm^2.

quantity of Zn will be ejected upon absorbing photon energy and combine with each other to form Zn^0.

3.3.3 Results analysis of EXAFS spectra

EXAFS spectra analysis of the products was carried out in order to further determine the chemical states of Zn species in the products. The major species of Zn were quantified with LCF using a collection of reference materials, including Zn^0, ZnS, ZnO, and $ZnSO_4$. The EXAFS spectra of the samples and reference materials were recorded in transmission mode. The spectra were processed and analyzed by the software codes Athena. Figure 9 shows the EXAFS spectra of the fresh samples prepared with a laser fluence of 7.76 and 15.52 J/cm^2, respectively.

According to Fig. 9, Zn^0 was generated in the products under the irradiation of different laser parameters. The fraction of Zn^0 in the products was determined to be ~6.2% when the pulse repetition frequency was 20 kHz and laser fluence was 7.76 J/cm^2, while the fraction of Zn^0 was 8.9% when the pulse repetition frequency was 60 kHz and laser fluence was 15.52 J/cm^2. The results are consistent with the XPS analysis shown in Fig. 6.

3.4 Economic comparison between optical metallurgy and traditional metallurgy for zinc production

For a traditional zinc metallurgy plant with an annual production capacity of 100,000 t, the infrastructure investment is ~1.62 billion yuan RMB. Among, the roasting and sulfuric acid production system costs ~440 million yuan RMB, the wet electrolysis system costs ~1 billion yuan RMB, and the leaching slag treatment rotary kiln system costs ~180 million yuan RMB. In the operational cost part, the overall cost is 19,000 yuan RMB per ton zinc. Among, the price of zinc concentrate is 15,000 yuan RMB per ton (ore powder after flotation enrichment with grade of 50% and water content of 13%). The operational cost is 4,000 yuan RMB per ton zinc including roasting, leaching, purification, electrolysis and waste treatment. Therefore, the annual operational cost of a traditional zinc metallurgy plant with an annual capacity of 100,000 t is 1.9 billion yuan RMB.

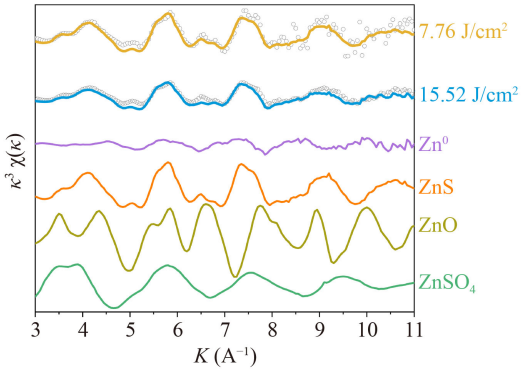

Fig. 9 Zn k^3-weighted extended X-ray absorption fine structure (EXAFS) spectra of the products prepared with a laser fluence of 7.76 J/cm^2 (20 kHz) and 15.52 J/cm^2 (60 kHz), respectively. The experimental data are shown as circles, the solid lines represent the LCF results, and the spectra of the reference materials

For the optical zinc metallurgy plant with an annual capacity of 100,000 t to be established, the infrastructure investment is ~2.6 billion yuan RMB, including ~2 billion yuan RMB for the laser metallurgy system (355 nm, 20 W) and ~600 million yuan RMB for the inert gas protection system. Its operational cost is 16,700 yuan RMB per ton zinc. Among, the price of zinc concentrate is 15,000 yuan RMB per ton zinc. The costs of electricity consumption and solid waste disposal are 900 and 800 yuan RMB, respectively, per ton zinc. Therefore, the annual operational cost of an optical zinc metallurgy plant with an annual production capacity of 100,000 t is 1.67 billion yuan RMB.

A preliminary economic analysis for the two plants is performed using the annual-cost (AC) approach, with the annual interest rate being 15% and life span of the fixed asset being ten years. It turns out AC for the traditional zinc metallurgy plant is 2.228 billion yuan RMB, and 2.188 billion yuan RMB for the optical zinc metallurgy plant. Therefore, the optical metallurgy is advantageous in terms of economic cost. In addition to the personal injuries caused by hazardous slag collapse, human health damages caused by acid mist and so on in the traditional zinc metallurgy plants are not included in the above analysis, since it is difficult to quantify economically these injuries and damages. The greenhouse gas generated by high temperature roasting is not listed in the terms of economical calculation either. It is necessary to point out the above economic analysis is calculated on the basis that optical metallurgy technology is fully matured. However, the technology is currently in laboratorial level. A huge amount of further studies are needed to realize, for the optical zinc metallurgy technology, the pilot scale plant and finally the full-scale plant.

4 Conclusions

This study demonstrated that Zn^0 can be produced by decomposing ZnS using laser irradiation under an inert argon gas atmosphere. This process does not require high temperatures and produces no greenhouse gases or pollutants. Our results are encouraging for the prospect for optical metallurgy. The development of optical metallurgy can reduce the pollutants produced by the electrolytic zinc industry from the source, mitigating environmental hazards and achieving cleaner production and green development. Although the proposed optical metallurgy method was only a preliminary attempt, its

success represents an innovative and promising new technology for the zinc metallurgy industry to reduce energy consumption and promote the environmental goals of reaching peak carbon emissions and, ultimately, carbon neutrality.

Acknowledgements This work was supported by the National Natural Science Foundation of China (Nos. 52174385 and 41877392), and Fundamental Research Funds for the Central Universities, Tongji University (No. 22120220166).

Conflict of Interests The authors Ning Duan and Fuyuan Xu are Editorial Board Members of *Frontiers of Environmental Science & Engineering*. The authors declare that the research was conducted in the absence of any commercial or financial relationships that could be construed as a potential conflict of interest.

Electronic Supplementary Material Supplementary material is available in the online version of this article at https://doi.org/10.1007/s11783-024-1767-8 and is accessible for authorized users.

References

Achehboune M, Khenfouch M, Boukhoubza I, Leontie L, Doroftei C, Carlescu A, Bulai G, Mothudi B, Zorkani I, Jorio A (2022). Microstructural, FTIR and Raman spectroscopic study of rare earth doped ZnO nanostructures. Materials Today: Proceedings, 53: 319–323

Ale Ebrahim H, Jamshidi E (2004). Energy Conversion and Management, 45(3): 345–363

Chuayboon S, Abanades S (2023). Solar metallurgical process for high-purity Zn and syngas production using carbon or biomass feedstock in a flexible thermochemical reactor. Chemical Engineering Science, 271: 118579

Du Q Z, Ren E Y (1995). A new attempt of laser application: laser metallurgy. Journal of Kunming Institute of Technology, 1: 96

Feng L P, Zhang L X, Chen X, Zhang C X, Mao G J, Wang H (2022). A visible light-driven photoelectrochemical sensor for mercury (II) with "turn-on" signal output through *in-situ* formation of double type-II heterostructure using CdS nanowires and ZnS quantum dots. Chemical Engineering Journal, 441: 136073

Feng Y, Liu Z Q, Yi X S (2000). Co-occurrence of photochemical and thermal effects during laser polymer ablation via a 248-nm excimer laser. Applied Surface Science, 156(1–4): 177–182

Griessacher T, Antrekowitsch J, Steinlechner S (2012). Charcoal from agricultural residues as alternative reducing agent in metal recycling. Biomass and Bioenergy, 39: 139–146

Jiang G F, Zhu B J, Sun J Z, Liu F, Wang Y Q, Zhao C C (2023). Enhanced activity of ZnS (111) by N/Cu co-doping: accelerated degradation of organic pollutants under visible light. Journal of Environmental Sciences (China), 125: 244–257

Jiang H Q, Jin S Y, Wang C, Ma R Q, Song Y Y, Gao M Y, Liu X T, Shen A G, Cheng G J, Deng H X (2019). Nanoscale laser metallurgy and patterning in air using MOFs. Journal of the American Chemical Society, 141(13): 5481–5489

Keshav R, Mg M (2018). Photoluminescence and Raman spectroscopic analysis of PV deposited ZnS thin films. Materials Research Bulletin, 105: 360–367

Kumar P, Rao G K (2022). Comprehensive analysis of microstructural, optical and electrical properties of ZnS thin films deposited by cost effective SILAR technique. Materials Today: Proceedings, 65(1): 380–384

Kumar V P, Pradeep C, Raj Sha M M, Radhakrishnan P, Mujeeb A (2023). Band-gap dependence of three-photon absorption in NiO nanoparticles synthesized at different calcination temperatures. Optics & Laser Technology, 158(Part A): 108809

Low J X, Dai B Z, Tong T, Jiang C J, Yu J G (2019). *In situ* irradiated X-ray photoelectron spectroscopy investigation on a direct Z-scheme TiO_2/CdS composite film photocatalyst. Advanced Materials, 31(6): 1802981

Major K J, Florea C M, Poutous M K, Busse L E, Sanghera J S, Aggarwal I D (2014). Surface transmission enhancement of ZnS via continuous-wave laser microstructuring. Laser-Based Micro- and Nanoprocessing VIII, 8968: 896810

Meng A, Huang T Q, Li H Y, Cheng H, Lin Y S, Zhao J, Li Z J (2021). Sulfur vacancies and morphology dependent sodium storage properties of MoS_{2-x} and its sodiation/desodiation mechanism. Journal of Colloid and Interface Science, 589: 147–156

Naik S S, Lee S J, Theerthagiri J, Yu Y, Choi M Y (2021). Rapid and highly selective electrochemical sensor based on ZnS/Au-decorated f-multi-walled carbon nanotube nanocomposites produced via pulsed laser technique for detection of toxic nitro compounds. Journal of Hazardous Materials, 418: 126269

Okano K, Hsu H Y, Li Y K, Masuhara H (2016). *In situ* patterning and controlling living cells by utilizing femtosecond laser. Journal of Photochemistry and Photobiology C, Photochemistry Reviews, 28: 1–28

Omran M, Fabritius T, Heikkinen E P, Chen G (2018). Dielectric properties and carbothermic reduction of zinc oxide and zinc ferrite by microwave heating. Royal Society Open Science, 1–16: 170710

Qi C C, Ye L P, Ma X T, Yang D L, Hong J L (2017). Life cycle assessment of the hydrometallurgical zinc production chain in China. Journal of Cleaner Production, 156: 451–458

Roychowdhury A, Pati S P, Kumar S, Das D (2014). Effects of magnetite nanoparticles on optical properties of zinc sulfide in fluorescent-magnetic Fe_3O_4/ZnS nanocomposites. Powder Technology, 254: 583–590

Scocioreanu M, Baibarac M, Baltog I, Pasuk I, Velula T (2012). Photoluminescence and Raman evidence for mechanico-chemical interaction of polyaniline-emeraldine base with ZnS in cubic and hexagonal phase. Journal of Solid State Chemistry, 186: 217–223

Shee N K, Adekunle F A O, Verma R, Kumar D, Datta D (2015). A

copper(II) complex with a Cu-S-8 bond. Attenuated total reflectance, electron paramagnetic resonance, resonance Raman and atoms-in-molecule calculations. Spectrochimica Acta. Part A: Molecular and Biomolecular Spectroscopy, 151(5): 96–99

Wagner C D, Naumkin A V, Kraut-Vass A, Allison J W, Powell C J, Rumble J R Jr (2012). NIST X-ray Photoelectron Spectroscopy Database, NIST Standard Reference Database 20, Version 4.1 (Web Version), U.S. Department of Commerce

Waltrovitz R R, Qian G J, de Groot F, Quinton J S, Harmer S L (2022). Influence of Co:Fe:Ni ratio on cobalt Pentlandite's electronic structure and surface speciation. Minerals Engineering, 190: 107935

Xiang H Q, Zhou Z C, Yang Y, Yu Z H, Liu J G (2022). Fabrication of metallic patterns on ordinary polymer substrates by laser direct activation and electroless plating. Surfaces and Interfaces, 33: 102209

Yang C, Wang J, Wang R, Zhu W, Zhang L, Du T, Sun J, Zhu M Q, Shen Y, Wang J (2023). Efficient hollow cubic Co_9S_8@defective ZnS/g-C_3N_4 for multi-pollutants removal via cascade Z-scheme heterojunction. Applied Catalysis B: Environmental, 322: 122084

Yang H, Huang X J, Hu J L, Thompson J R, Flower R J (2022). Achievements, challenges and global implications of China's carbon neutral pledge. Frontiers of Environmental Science & Engineering, 16(8): 111

Ye G, Wang W, Fan D, He P (2021). Effects of femtosecond laser micromachining on the surface and substrate properties of poly-lactic acid (PLA). Applied Surface Science, 538: 148117

Young Maeng J, Hyun Yang J, Ji Jang H, Hee Joo M, Jun Kim Y, Kyun Rhee C, Sohn Y (2023). Electrocatalytic syngas and photocatalytic long-chain hydrocarbon productions by CO_2 reduction over ZnO and Zn-based electrodes. Applied Surface Science, 609: 155349

Zhang H, Cui Q Q, Xu L L, Jiao A X, Tian Y, Liu X D, Li S, Li H S, Chen M, Chen F (2020). Blue laser-induced photochemical synthesis of CuAg nanoalloys on h-BN supports with enhanced SERS activity for trace-detection of residual pesticides on tomatoes. Journal of Alloys and Compounds, 825: 153996

Zhang X, Xuan Y, Wang B, Gao C, Niu S L, Zhao G J, Wang D, Li J H, Lu C M, Crittenden J C (2022b). Precise regulation of acid pretreatment for red mud SCR catalyst: targeting on optimizing the acidity and reducibility. Frontiers of Environmental Science & Engineering, 16(7): 88

Zhang Y W, Zhang Y J, Zhu H X, Zhou P X, Liu S, Lei X L, Li Y H, Li B, Ning P (2022a). Life cycle assessment of pollutants and emission reduction strategies based on the energy structure of the nonferrous metal industry in China. Energy, 261(15): 125148

Zhou T S, Wan H, Liu M K, Wu Q Y, Fan Z C, Zhu Y C (2022). Regulating uniform nucleation of ZnS enables low-polarized and high stable aqueous Zn-S batteries. Materials Today. Energy, 27: 101025